# Suspension electrolyte with modified $Li^+$ solvation environment for lithium metal batteries

Mun Sek Kim[1,2,6], Zewen Zhang[1,6], Paul E. Rudnicki[2], Zhiao Yu[2,3], Jingyang Wang[1,4], Hansen Wang[1], Solomon T. Oyakhire[2], Yuelang Chen[2,3], Sang Cheol Kim[1], Wenbo Zhang[1], David T. Boyle[1,3], Xian Kong[2], Rong Xu[1], Zhuojun Huang[1,2], William Huang[1], Stacey F. Bent[2], Lin-Wang Wang[4], Jian Qin[2], Zhenan Bao[2] and Yi Cui[1,5] ✉

**Designing a stable solid–electrolyte interphase on a Li anode is imperative to developing reliable Li metal batteries. Herein, we report a suspension electrolyte design that modifies the $Li^+$ solvation environment in liquid electrolytes and creates inorganic-rich solid–electrolyte interphases on Li. $Li_2O$ nanoparticles suspended in liquid electrolytes were investigated as a proof of concept. Through theoretical and empirical analyses of $Li_2O$ suspension electrolytes, the roles played by $Li_2O$ in the liquid electrolyte and solid–electrolyte interphases of the Li anode are elucidated. Also, the suspension electrolyte design is applied in conventional and state-of-the-art high-performance electrolytes to demonstrate its applicability. Based on electrochemical analyses, improved Coulombic efficiency (up to ~99.7%), reduced Li nucleation overpotential, stabilized Li interphases and prolonged cycle life of anode-free cells (~70 cycles at 80% of initial capacity) were achieved with the suspension electrolytes. We expect this design principle and our findings to be expanded into developing electrolytes and solid–electrolyte interphases for Li metal batteries.**

Li metal ($Li^0$) is an ideal anode material due to its low density (0.534 g $cm^{-3}$), high theoretical capacity (3,860 mAh $g^{-1}$ and 2,061 mAh $cm^{-3}$), low standard electrode potential (−3.04 V versus the standard hydrogen electrode) and compatibility with lithiated and unlithiated cathode materials[1–4]. Achieving stable and reversible $Li^+$ migration between the cell electrodes poses a formidable challenge due to the existence of an intricate solid–electrolyte interphase (SEI) at the $Li^0$ anode and electrolyte interface[5]. Designing stable SEIs on a $Li^0$ anode is the key to success in developing $Li^0$ batteries (LMBs) as the properties of SEIs largely dictate the electrochemical performances of the $Li^0$ anode[6–8]. However, the control and understanding of the SEI on the $Li^0$ anode remain challenging due to heterogeneous composition[9], nanostructure[5], hypersensitivity to the ambient environment[6,8] and spatiotemporal evolution[10] of the SEIs.

As the SEI evolution on the $Li^0$ anode is directly associated with electrolyte formulations, various electrolyte modifications (blending different solvents[11–13] and salts[14], designing new solvents[15], varying salt concentrations[16–20] and using solvent-specific diluents[21–23]) have been studied to delineate different SEI properties that influence the electrochemical performances of the $Li^0$ anode[5]. The consensus is that the inorganic-rich SEIs on the $Li^0$ anode promote superior electrochemical performances[15–23]. Since inorganic and organic contents of SEIs were closely linked to the electrolyte $Li^+$ solvation environment[5], understanding and modifying electrolyte $Li^+$ solvation structures has become an important driver for developing electrolytes for LMBs.

To date, the pursuit of forming inorganic-rich SEIs has been achieved by increasing $Li^+$–anion coordination (maximizing contact ion pairs and ionic aggregates)[16–23] and weakening $Li^+$–solvent coordination (minimizing solvent-separated ion pairs)[15,24] in the electrolyte $Li^+$ solvation shells. The general approaches to increase contact ion pairs and ionic aggregates in the $Li^+$ solvation shells are to use high concentration electrolytes (HCEs)[16–20] or combine HCEs with solvent-specific diluents to make localized HCEs (LHCEs)[15–23]. As the coordination between $Li^+$ and solvent is affected by the polarity and/or donor number of solvents[5,17], designing a new solvent with functional structures has enabled the decrease in $Li^+$–solvent and increase in $Li^+$–anion coordinations that create inorganic-rich SEIs on the $Li^0$ anode[15].

Herein, we propose a suspension electrolyte design, a mixture of inorganic nanoparticles with liquid electrolytes, to understand the suspension's role in impacting the SEI evolution and the electrochemical performances of the $Li^0$ anode. Due to the ubiquitous presence of $Li_2O$ in both prevalent and inorganic-rich SEIs[5] of the $Li^0$ anode and to the low solubility of $Li_2O$ (ref. [25]), a $Li_2O$ suspension was scrutinized to elucidate the working mechanism of the $Li_2O$ suspension in the electrolyte and to reveal features of $Li_2O$ that relate to SEIs of the $Li^0$ anode. To systematically study the suspension electrolytes, we investigated a reference carbonate electrolyte (RCE; 1 M $LiPF_6$ in ethylene carbonate (EC)/diethylene carbonate (DEC)/10 vol% fluoroethylene carbonate (FEC)) that is widely studied as a standard electrolyte for the $Li^0$ anode and SEIs[5,7,8,10,26]; a reference fluorinated electrolyte (RFE; 1 M lithium bis(fluorosulfonyl) imide (LiFSI) in fluorinated 1,4-dimethoxylbutane (FDMB)) that is one of the state-of-the-art electrolytes with a modified $Li^+$ solvation structure[15]; and a reference LHCE (RLHCE; 1 M LiFSI in dimethoxyethane (DME)/1,1,2,2-tetrafluoroethyl-2,2,3,3-tetrafluoropropyl ether (TTE; 0.78:0.22 v/v)) that exhibits a unique $Li^+$ solvation environment[21]. The suspension electrolytes were prepared by adding

[1]Department of Materials Science and Engineering, Stanford University, Stanford, CA, USA. [2]Department of Chemical Engineering, Stanford University, Stanford, CA, USA. [3]Department of Chemistry, Stanford University, Stanford, CA, USA. [4]Materials Sciences Division, Lawrence Berkeley Laboratory, Berkeley, CA, USA. [5]Stanford Institute for Materials and Energy Sciences, SLAC National Accelerator Laboratory, Menlo Park, CA, USA. [6]These authors contributed equally: Mun Sek Kim, Zewen Zhang. ✉e-mail: yicui@stanford.edu

~80–100 nm $Li_2O$ nanoparticles into RCE, RFE and RLHCE, which were then referred to as the suspension carbonate electrolyte (SCE), suspension fluorinated electrolyte (SFE) and suspension LHCE (SLHCE), respectively. Through theoretical and empirical analyses on the $Li_2O$ suspension electrolyte, several key features of $Li_2O$ were identified: (1) $Li_2O$ modifies the $Li^+$ solvation environment through the interfacial interactions between the $Li_2O$ surface and its surrounding $Li^+$ solvation shells of the liquid electrolyte, (2) $Li_2O$ creates a weakly solvating environment by decreasing $Li^+$–solvent and increasing $Li^+$–anion coordinations, (3) $Li_2O$ facilitates desolvation of solvated $Li^+$, (4) $Li_2O$ attracts fluorinated species and dissociated $Li^+$, (5) $Li_2O$ induces inorganic-rich and anion-derived SEIs on the $Li^0$ anode, (6) $Li_2O$ promotes a formation of temporally and electrochemically stable interphases on the $Li^0$ anode, (7) $Li_2O$ suppresses dendritic growth of $Li^0$ and (8) $Li_2O$ is a beneficial inorganic material for the $Li^0$ anode. Importantly, these findings help to explain previously reported improved $Li^0$ anode performances with the multi-layered $Li_2O$ SEI[7,8,27,28]. Despite the veiled formation mechanism of multi-layered[7,8,27,28], amorphous[29] and crystalline[30–32] $Li_2O$ in SEIs, increasing $Li_2O$ content in SEIs improves the $Li^+$ migration stability of the $Li^0$ anode[7,8,27–32], a result in which the previous findings agree with the outcome of this study. We demonstrate an improved Coulombic efficiency (CE) of ~99.7% for $Li^0$ and electrochemical performances of anode-free full cells with the suspension electrolyte design. As a corollary, the suspension electrolyte design adds extra layers to the fundamental understanding of the inorganics in SEIs (that is, $Li_2O$), provides a comprehensive electrolyte engineering strategy and guides the development of electrolytes for LMBs.

## Analyses of the suspension electrolyte

The SEI evolution of $Li^0$ depends on the $Li^+$ solvation environment of electrolytes and solubility of decomposed electrolyte species (Supplementary Note 1). We found that the major impact of the $Li_2O$ suspension electrolyte originates from the modification of the $Li^+$ solvation environment in the vicinity of the $Li_2O$ surface. Therefore, one of the criteria for optimizing the suspension electrolyte effect is to have the suspension laying out near the surface of the $Li^0$ anode to affect the SEI evolution. Furthermore, we hypothesize that saturating $Li_2O$ in the suspension electrolyte is also a contributing factor that impacts the SEI evolution of the $Li^0$ anode as $Li_2O$ is least soluble, but not completely insoluble, in electrolytes[25], among the prevalent inorganics ($Li_2O$, $Li_2CO_3$ and LiF) observed in SEIs of the $Li^0$ anode[5]. By synthesizing the previous findings and key results from this work, we portray SEI evolutions on the $Li^0$ anode with liquid and suspension electrolytes in Fig. 1a,b. Figure 1a (Supplementary Fig. 1) depicts the SEI evolution of a conventional liquid electrolyte (Supplementary Note 2) on a $Li^0$ anode that forms an organic-rich SEI, while Fig. 1b (Supplementary Fig. 2) interprets the altered SEI evolution on a $Li^0$ anode induced by the modified $Li^+$ solvation environment in the $Li_2O$ suspension electrolyte (Supplementary Note 3), which creates an inorganic-rich SEI on the $Li^0$ anode.

To access the electrochemical features of the RCE and SCE, the CE measurements[33] from Li|Cu cells were conducted (Fig. 1c). The CE of SCE (97.5%) exhibited an ~4% increase relative to that of RCE (93.4%). The nucleation overpotentials[34,35] for RCE (99.5 mV) and SCE (41.2 mV) were also calculated (Fig. 1c), in which SCE exhibited a lower energy barrier to form $Li^0$ nuclei. Averaged CEs and nucleation overpotentials with standard errors are reported in Fig. 1d. It is apparent that the improved CE and reduced nucleation overpotential with SCE arise from the $Li_2O$ suspension, as the identical liquid electrolyte was used for RCE and SCE. The major determinants of CEs are correlated with topography[10] of $Li^0$ electrodeposits and SEI characteristics[7]. The scanning electron microscopy (SEM) images in Fig. 1e,f provide a clear physical insight into the morphological features of $Li^0$ electrodeposits on Cu with RCE and SCE. The resulting morphologies with RCE exhibited high surface area and dendritic $Li^0$ electrodeposits on Cu (Fig. 1e), which is a common signature of standard carbonate-based electrolytes[7,8,26]. On the contrary, denser and bulkier $Li^0$ electrodeposits on Cu were observed with SCE (Fig. 1f). The lower surface area and bulkier $Li^0$ electrodeposits obtained with SCE (Fig. 1f) compared with RCE (Fig. 1e) explain the improvement of the CE and reduced nucleation overpotential. It is known that a substantial number of charges are consumed irreversibly to form SEIs on a $Li^0$ anode surface, indicating an inversely proportional relationship between CE and the surface area of $Li^0$ electrodeposits[1,33]. Furthermore, a smaller nucleation overpotential thermodynamically favours forming larger sizes of $Li^0$ nuclei, eventually leading to bulkier $Li^0$ electrodeposits[35]. Thus, the lower surface area and bulkier $Li^0$ electrodeposits achieved with SCE (Fig. 1f) than with RCE (Fig. 1e) support CE improvement and reduced nucleation overpotential (Fig. 1c,d).

To investigate the nanoscopic origin of the performance enhancement of SCE, we utilized cryogenic scanning transmission electron microscopy (cryo-STEM)[6,8] to probe the nanostructure and local chemistry of the compact SEI derived from RCE (RCE-SEI) and from SCE (SCE-SEI). The $Li^0$ electrodeposits on the Cu transmission electron microscopy (TEM) grid with RCE (Fig. 2a) and SCE (Fig. 2b) confirm the consistent $Li^0$ morphology observed in Fig. 1e,f. The high-resolution cryo-TEM images of RCE-SEI (Fig. 2c) and SCE-SEI (Fig. 2d) reveal the thinner and $Li_2O$-richer (Supplementary Fig. 1) characteristics of SCE-SEI.

Cryo-STEM electron energy loss spectroscopy (EELS) was performed to identify the differences in the chemistries of RCE-SEI and SCE-SEI. In the oxygen K-edge map, a more abundant distribution of oxygen elements was identified for SCE-SEI (Fig. 2e,f). Moreover, carbon K-edge (Fig. 2g) and oxygen K-edge (Fig. 2h) fine structures of RCE-SEI and SCE-SEI were compared to delineate the SEI chemistries. For SCE-SEI, a lower C–H signal (around 286 eV) and higher C=O signal (around 290 eV) were obtained relative to RCE-SEI[6,10]. The lower C–H and higher C=O signals in the carbon K-edge fine structure of SCE-SEI signify relatively lower organic content in SCE-SEI than in RCE-SEI[6,10]. This claim was further evidenced by observing the oxygen K-edge fine structure in Fig. 2h. The absence of the peak around 531 eV in the oxygen K-edge fine structure (Fig. 2h) of SCE-SEI indicates the $Li_2O$-dominated SEI chemistry[6,36], in which the result matches with the abundant $Li_2O$ observed in Supplementary Fig. 1b. Based on the cryo-STEM and EELS analyses, SCE-SEI was inorganic rich, particularly in $Li_2O$. The enrichment of $Li_2O$ in SCE-SEI is corroborated in Supplementary Note 4 and Supplementary Fig. 2. We also speculate that the different morphological features of $Li^0$ electrodeposits with RCE and SCE (Figs. 1e,f and 2a,b) are possibly related to the high surface energy of $Li_2O$ in SEIs (Supplementary Fig. 3), as the high-surface-energy SEI has been known to suppress the formation of $Li^0$ dendrites[37] (Supplementary Note 5). The different evolution of SEIs observed with RCE and SCE strongly suggests that the $Li^+$ solvation environment in RCE and SCE must be different due to an interplay between the SEI evolution on $Li^0$ and in the $Li^+$ solvation environment of electrolytes[5].

## $Li^+$ solvation environment of the suspension electrolyte

Molecular dynamics (MD) simulations were conducted to understand the $Li^+$ solvation environment in RCE and SCE, which impacts the SEI formation on the $Li^0$ anode[5] (Fig. 3). Snapshots of simulated RCE and SCE systems are shown in Fig. 3a, and the normalized density profiles of the electrolyte species in SCE are plotted in Fig. 3b. Near the $Li_2O$ slab in SCE, the $Li^+$ solvation structure differs from that observed in RCE, as evidenced by clear peaks in the normalized density profile due to the strong adsorption and diffusion of $Li^+$ at the $Li_2O$ surface and the different coordination of electrolyte components to the $Li_2O$ surface (Fig. 3c). Furthermore,

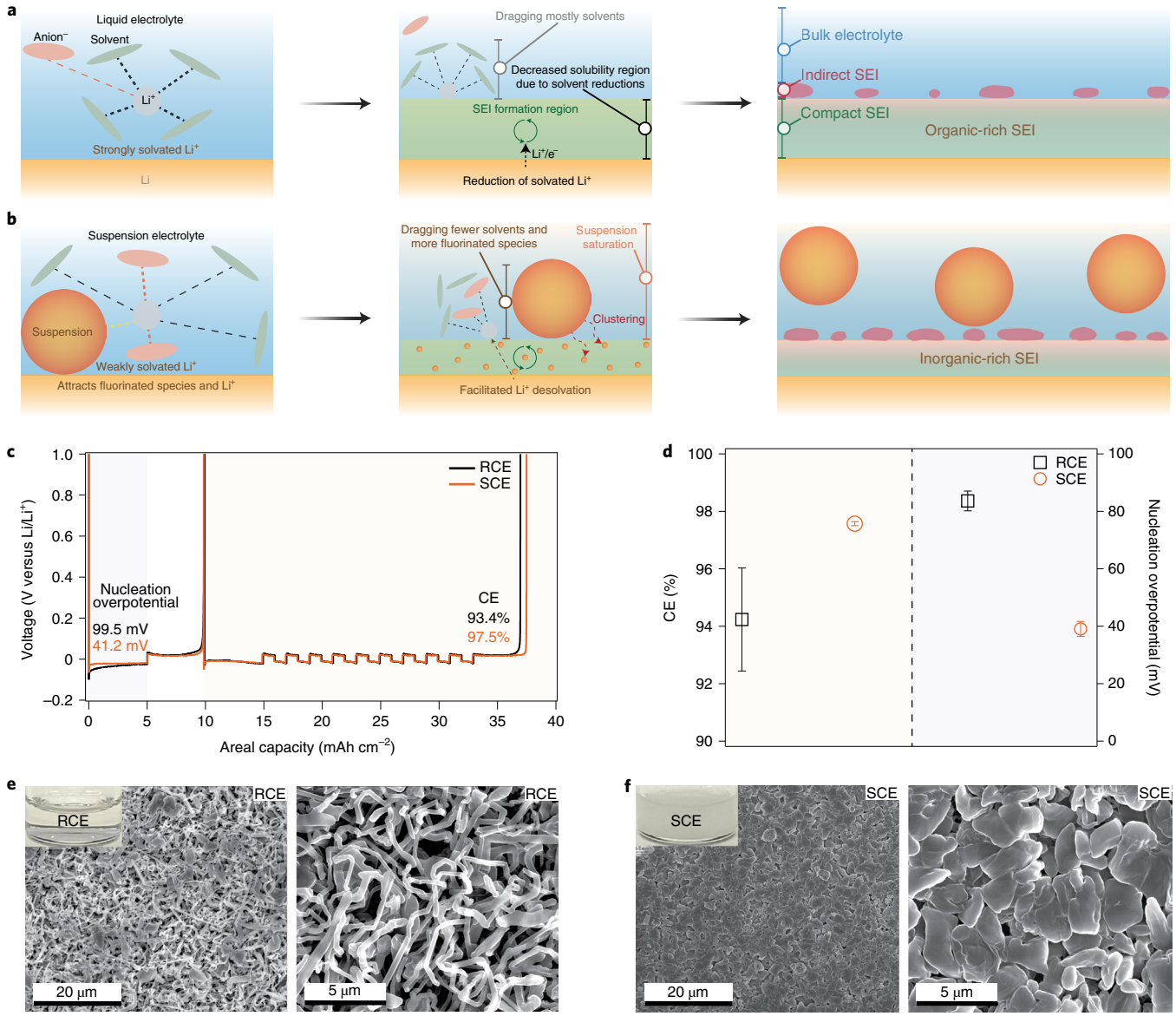


**Fig. 1 | Liquid and suspension electrolytes for the Li⁰ anode. a**, Schematic illustration for a conventional liquid electrolyte affecting the SEI evolution of the Li⁰ anode. The details for each of the subset schematics are provided in Supplementary Figure Caption 1. $e^-$, electron. **b**, Schematic illustration for a suspension electrolyte affecting the SEI evolution of the Li⁰ anode. The details for each of the subset schematics are provided in Supplementary Figure Caption 2. **c**, Representative voltage profiles from Li|Cu cells with RCE and SCE for measuring CE and nucleation overpotential at 0.5 mA cm$^{-2}$. The background colours represent where the CE and nucleation overpotential were calculated. **d**, Averaged CE and nucleation overpotential values from four identical Li|Cu cells with RCE and SCE. The background colours represent the regions where CE and nucleation overpotential were calculated from **c**. The averaged CE and nucleation overpotential values of the electrolytes with standard errors are RCE (94.23 ± 1.79% and 83.65 ± 3.43 mV) and SCE (97.57 ± 0.07% and 39.10 ± 2.61 mV). The error bars were calculated by taking the standard errors from the measurements with four identical samples. **e**, Low (left) and high (right) magnification SEM images of Li⁰ electrodeposit on Cu from the Li|Cu cell with RCE at 1 mA cm$^{-2}$ and 1 mAh cm$^{-2}$. The inset image shows the physical image of RCE. **f**, Low (left) and high (right) magnification SEM images of Li⁰ electrodeposit on Cu from the Li|Cu cell with SCE at 1 mA cm$^{-2}$ and 1 mAh cm$^{-2}$. The inset image shows the physical image of SCE.

density functional theory (DFT) calculations were performed to figure out the most favourable Li adatom interaction sites for the $Li_2O(111)$ surface. According to Fig. 3d, $Li_2O(111)$ surface site 1 (−0.93 eV) provided the most favourable Li adatom adsorption, demonstrating a favoured $Li^0$–$O_{Li_2O}$ interaction, where $O_{Li_2O}$ is the oxygen in $Li_2O$ (Supplementary Note 6). These simulation results revealed the existence of $Li^{+/0}$–$Li_2O$ interactions that could influence the $Li^+$ solvation environment. Moreover, FEC also showed a larger concentration near the $Li_2O$ surface relative to EC. Density profiles of electrolyte species in RCE and away from the $Li_2O$ surface in SCE exhibited a similar behaviour (Supplementary Fig. 4). In other words, the effect of $Li_2O$ suspension comes from the interfacial interaction between $Li_2O$ and its neighbour $Li^+$ solvation shells of the liquid electrolyte.

Radial distribution functions (RDFs) were used to analyse the relative compositions of electrolyte species in the first $Li^+$ solvation shell of SCE (Fig. 3e) and RCE (Fig. 3f). The fluorinated species (FEC and $PF_6^-$) were enriched in the first $Li^+$ solvation shell of SCE relative to the non-fluorinated carbonates (EC and DEC), while RDFs of $Li^+$ farther from the $Li_2O$ surface exhibited similar

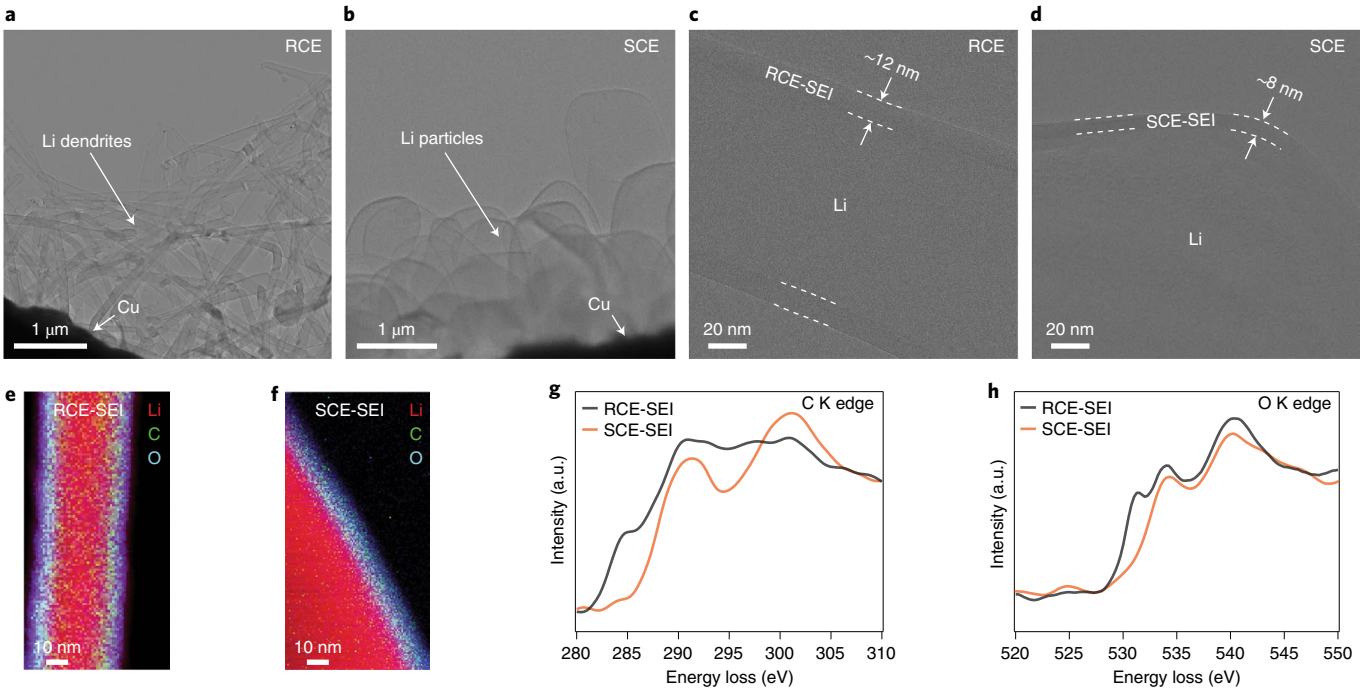


**Fig. 2 | Compact SEI analysis via cryo-STEM. a**,**b**, Low magnification cryo-STEM images of $Li^0$ electrodeposits on Cu TEM grid with RCE (**a**) and SCE (**b**). The samples were prepared from a Li|Cu-TEM-grid cell at 1 mA $cm^{-2}$ and 0.1 mAh $cm^{-2}$. The arrows indicate the morphology of the $Li^0$ electrodeposit with RCE and SCE. **c**,**d**, High magnification cryo-STEM images of RCE-SEI (**c**) and SCE-SEI (**d**). SEI regions and the thicknesses are illustrated with dashed lines and arrows. **e**,**f**, Large area cryo-STEM EELS mapping of Li (red), C (green) and O (sky blue) around RCE-SEI (**e**) and SCE-SEI (**f**). **g**, Carbon K-edge fine structure of RCE-SEI and SCE-SEI obtained from EELS. **h**, Oxygen K-edge fine structure of RCE-SEI and SCE-SEI obtained from EELS.

characteristics to those in RCE (Supplementary Fig. 5). This is quantified by examining the composition of the first $Li^+$ solvation shell in each environment, revealing that both FEC and $PF_6^-$ were increased by percentage in the first $Li^+$ solvation shell near the $Li_2O$ surface in SCE, while EC was more prevalent in the $Li^+$ solvation shells of RCE (Fig. 3g and Supplementary Fig. 6). The molecular origin of the fluorinated species enrichment at the $Li_2O$ surface is explained in Supplementary Note 7 with Supplementary Figs. 7 and 8. Consequently, the enrichment of fluorinated species in the $Li^+$ solvation shells near the $Li_2O$ surface explains the increased content of LiF and F/O counterparts, which promotes stable $Li^+$ migration[5,38], observed around $Li_2O$ in SEIs of the $Li^0$ anode due to the preferential decomposition of fluorinated species[26,30]. Also, these results verify the desirable features of the multi-layered $Li_2O$ SEIs observed in previous works[7,8,27,28]. Overall, three essential features of the $Li_2O$ in the electrolyte were revealed by the simulations: (1) the $Li^+$ solvation environment changes (more anion and less solvent to $Li^+$ coordinations) near the surface of $Li_2O$, (2) the fluorinated species are enriched near the surface of $Li_2O$ and (3) dissociated $Li^+$ in the electrolyte is strongly adsorbed onto the $Li_2O$ surface.

The relative solvation energies of RCE and SCE were measured with an H-cell[39] comprised of symmetric $Li^0$ electrodes but asymmetric electrolytes to experimentally verify the features of $Li_2O$ attained from the simulations (Supplementary Note 8). Based on the solvation energy measurements with RCE and 20 wt% $Li_2O$ SCE (Fig. 4a), a smaller cell potential ($E_{cell}$) and more positive solvation energy were measured with 20 wt% $Li_2O$ SCE. This trend signifies that dissociated $Li^+$ in 20 wt% $Li_2O$ SCE became relatively weakly solvated. In other words, the $Li_2O$ suspension in the electrolyte decreases the $Li^+$–solvent coordination (facilitating desolvation of $Li^+$ in the solvation shell) and increases the $Li^+$–anion coordination (promoting anion-derived SEIs on the $Li^0$ anode)[39]. Furthermore, the solvation energies were measured with a larger $Li_2O$ particle (a $Li_2O$ microparticle) but equal weight percent in the electrolyte to examine the effect of the surface-area-to-volume ratio of the $Li_2O$ suspension (Supplementary Fig. 9). The same $E_{cell}$ and solvation energy trends were detected with 20 wt% $Li_2O$ microparticle; however, the change was smaller in magnitude (Supplementary Note 9). This substantiates that the $Li^+$ solvation environment change depends on the surface-area-to-volume ratio of the $Li_2O$ suspension in the electrolyte, which shows that the modification of the $Li^+$ solvation environment arises from the surface interactions of $Li_2O$. Thus, the solvation energy measurements experimentally proved the features of $Li_2O$ obtained from the simulation results (Supplementary Note 10).

The $^7Li$ NMR analysis[40] provides two important characteristics about the suspension electrolyte: (1) qualitatively confirming the altered $Li^+$ solvation environment in the suspension electrolyte and (2) determining the optimal suspension content in the suspension electrolyte. The $^7Li$ NMR spectra of RCE, 1–20 wt% $Li_2O$ SCE and 7 wt% $Li_2O$ in EC/DEC are shown in Fig. 4a. The upfield (shifting to lower parts per million, to the right) or downfield (shifting to higher parts per million, to the left) peak shifts describe the changes in the $Li^+$ solvation environment: the upfield and downfield peak shifts represent increased and decreased electron density around the nuclei of dissociated $Li^+$, respectively[40]. In Fig. 4a, the peak of SCE as a function of $Li_2O$ content gradually shifts to the upfield direction (increasing electron density of the solvated $Li^+$) as the $Li_2O$ suspension content increases. The upfield peak shifts, therefore, reflect increased $Li^+$ coordination with negatively charged species in the electrolyte. The simulation results (Fig. 3) and the solvation energy trend (Fig. 4a) illustrate that the upfield peak shifts stem from the increased $Li^+$–anion coordination, while $Li^+$–solvent coordination was relatively weakened. Also, the $Li^+$ density profile in Fig. 3c shows the surface adsorption of $Li^+$ onto $Li_2O$, in which the $Li^+$–$O_{Li_2O}$ interaction contributes to the upfield peak shifts as the oxygen

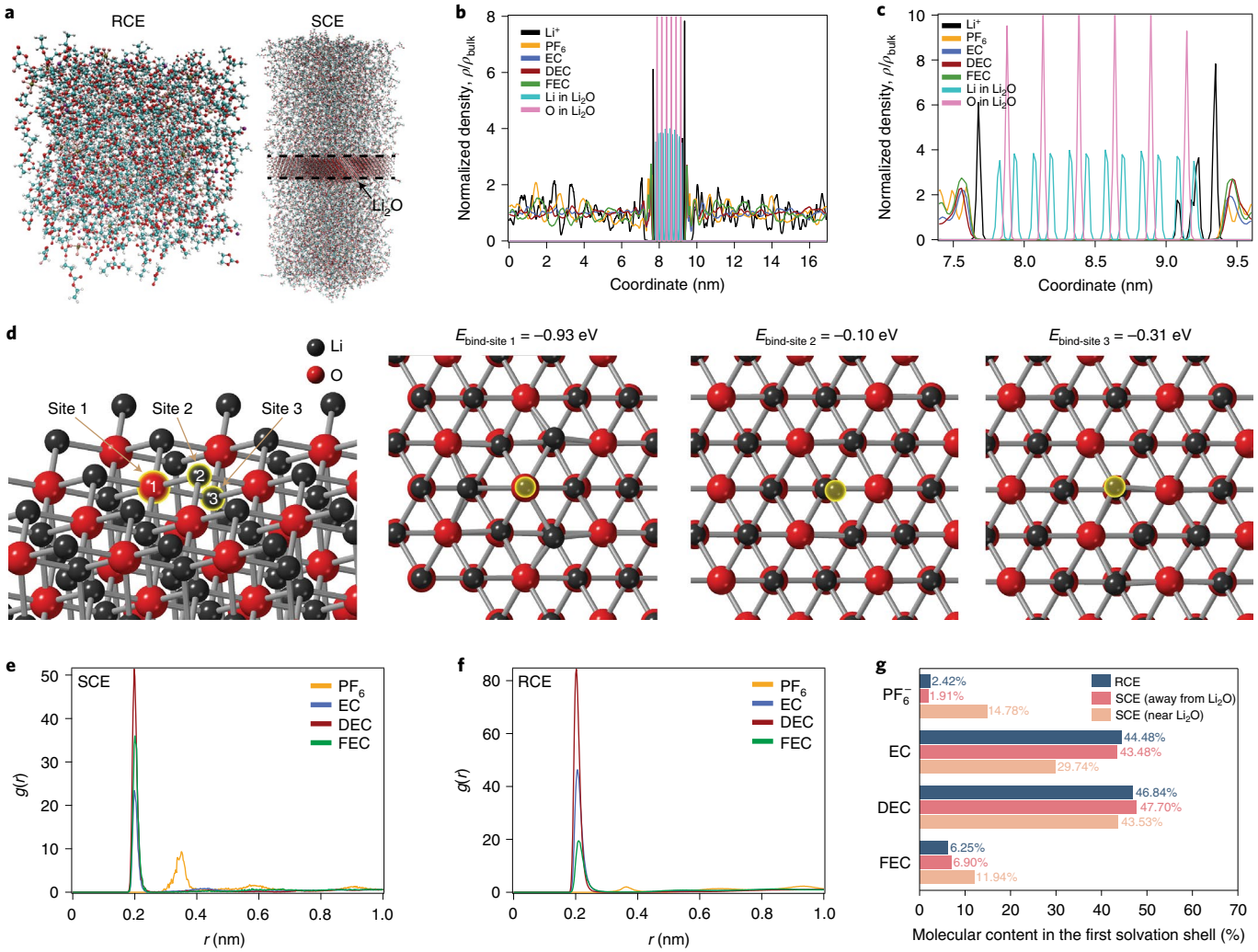


**Fig. 3 | Simulations for the $Li^+$ solvation environment of RCE and SCE. a**, Snapshots of MD simulations of molecular species ($Li^+$, $PF_6^-$, EC, DEC and FEC) for RCE and SCE. The colour codes for the images are oxygen (red), carbon (cyan), hydrogen (white), phosphorus (tan), fluorine (pink), $Li^+$ (purple) and Li in $Li_2O$ (grey). **b**, Density profiles of SCE with the $Li_2O$ slab. The ρ and $\rho_{bulk}$ represent density and bulk density of the specified species. **c**, Density profiles of SCE near the $Li_2O$ slab in **b**. **d**, Snapshots of Li adatom binding sites 1 to 3 on the $Li_2O$(111) surface. Sites 1, 2 and 3 refer to the Li adatom adsorbed close to the oxygen on the $Li_2O$ surface, the Li adatom adsorbed to the outward lithium on the $Li_2O$ surface and the Li adatom adsorbed to the inward lithium on the $Li_2O$ surface, respectively. The DFT-calculated binding energies of the Li adatom on site 1, site 2 and site 3 ($E_{bind\text{-}site\ 1}$, $E_{bind\text{-}site\ 2}$ and $E_{bind\text{-}site\ 3}$, respectively) were −0.93 eV, −0.10 eV and −0.31 eV, respectively. **e**, RDFs for the first $Li^+$ solvation shell of SCE near the $Li_2O$ slab. The $g(r)$ represents the radial distribution function. **f**, RDFs for the first $Li^+$ solvation shell of RCE. **g**, Calculated electrolyte species content in the first $Li^+$ solvation shell in the bulk of RCE and away from and near the $Li_2O$ slab of SCE.

is negatively charged. Furthermore, the peak shifts as a function of the $Li_2O$ suspension content in the electrolyte emphasize that the degree of the change in the $Li^+$ solvation environment depends on the absolute surface area and the surface-area-to-volume ratio of the $Li_2O$ suspension in the electrolyte (Supplementary Note 11 with Supplementary Fig. 10). Note that the absence of the peak in the spectra of 7 wt% $Li_2O$ in EC/DEC (Fig. 4b) confirms that the observed $Li^+$ peaks in RCE and 1–20 wt% $Li_2O$ SCE were the dissociated $Li^+$ from the salt, not $Li_2O$ suspension (Supplementary Note 12 with Supplementary Fig. 11). The amount of relative upfield peak shift is linear in suspension contents up to 7 wt% and increases steadily beyond 7 wt% (Fig. 4c), indicating that the effects of suspension on the $Li^+$ solvation environment is weakened above 7 wt% of $Li_2O$ loading (Supplementary Note 13 with Supplementary Fig. 12). Therefore, 7 wt% $Li_2O$ is considered as the optimal content for SCE and has been employed to measure the electrochemical properties of SCE. These $Li^+$ solvation environment analyses reveal that the $Li^+$ solvation environment gets modified near the surface of the $Li_2O$ suspension in the electrolyte. Moreover, this mechanism suggests that it is crucial to have the $Li_2O$ suspension in the vicinity of the $Li^0$ anode to deliver the effects; the $Li_2O$ suspension effects are further discussed in Supplementary Note 14 with Supplementary Figs. 13 and 14.

## $Li^0$ interphases with the suspension electrolyte

X-ray photoelectron spectroscopy (XPS) surface analysis on electrodeposited $Li^0$ was performed to extract more information about the indirect SEI (iSEI) region as XPS has high out-of-plane resolutions[26]. The elemental ratios of P/C, F/C, F/O and C/O, which help to track the origin of the sources to construct iSEIs (Supplementary Note 15), from iSEI with RCE (RCE-iSEI) and with SCE (SCE-iSEI) were calculated (Fig. 4d). Relatively higher P/C, F/C and F/O ratios and a lower C/O ratio were obtained for SCE-iSEI compared to that for RCE-iSEI. These ratios confirm that more anions were

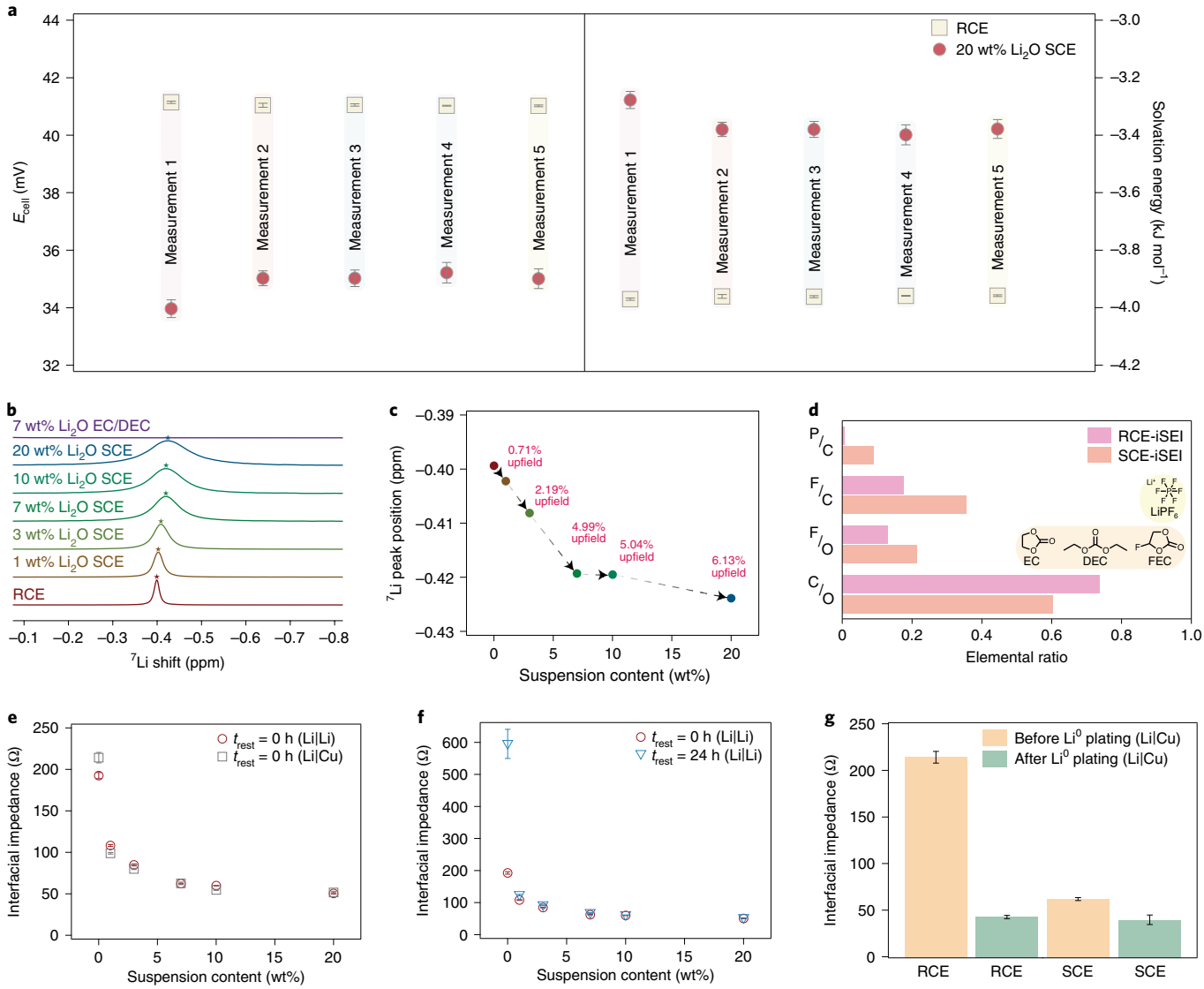


**Fig. 4 | Further analysis of the suspension electrolyte. a**, The potentiometric measurements of averaged cell potentials ($E_{cell}$, left half) and $Li^+$ solvation energies (right half) with standard errors for RCE and 20 wt% $Li_2O$ SCE. **b**, The $^7Li$ NMR spectra of RCE and 1 wt% to 20 wt% $Li_2O$ SCE. **c**, The $^7Li$ NMR peak positions retrieved from **b** with respect to the suspension contents. The relative peak shifts are indicated with the arrows. **d**, Elemental ratios of P/C, F/C, F/O and C/O on RCE-iSEI and SCE-iSEI obtained from XPS scans. The XPS scans were performed on electrodeposited $Li^0$ on Cu from Li|Cu cells with RCE and SCE at 1 mA $cm^{-2}$ and 1 mAh $cm^{-2}$. The insets represent electrolyte species that can be reduced to form iSEIs on the $Li^0$ anode. **e**, The interfacial impedance of Li|Li and Li|Cu cells with RCE and 1 wt% to 20 wt% SCE measured at $t_{rest} = 0$ h. The $t_{rest}$ value represents the cell resting time after cell assembly. **f**, The interfacial impedance of Li|Li cells with RCE and 1 wt% to 20 wt% SCE measured at $t_{rest} = 0$ h and $t_{rest} = 24$ h. **g**, The interfacial impedance measured before and after $Li^0$ electrodeposition on Cu from Li|Cu cells with RCE and SCE at 1 mA $cm^{-2}$ and 1 mAh $cm^{-2}$. Three identical samples were measured in **e**, **f** and **g** to obtain the averaged interfacial impedance values with standard errors.

decomposed in SCE-iSEI than the solvents, which agrees with the characteristics of the modified $Li^+$ solvation in SCE (Figs. 3 and 4a,b)[5,17] and validates higher contents of inorganic species in SCE-iSEI on $Li^0$. The high-resolution XPS spectra of P, C, O and F (Supplementary Fig. 15) revealed higher $Li_2O$ and LiF contents for SCE-iSEI than for RCE-iSEI. Additionally, it has been reported that $Li_2O$ in SEIs can act as a conduit for electron transfer as it is more receptive to electronic charge transfer from the $Li^0$ anode. The transferred electrons then participate to preferentially decompose anions that favour anion-derived species in SEIs on the $Li^0$ anode[41].

The electrochemical impedance spectroscopy of $Li^0$ electrodes was measured with RCE and ~1–20 wt% $Li_2O$ SCE (Fig. 4e,f) to evaluate the characteristics of the interphases that $Li^0$ forms with the $Li_2O$ suspension in the electrolyte. Collectively, Li|Li and Li|Cu cells were used to systematically verify the interfacial impedance trends (Fig. 4e, Supplementary Fig. 16 and Supplementary Table 1). A noticeable decrease of the interfacial impedances was observed with ~1–20 wt% $Li_2O$ SCE. The decrease of the interfacial impedance is attributed to the weakly solvating environment that may facilitate $Li^+$ desolvation induced by the $Li_2O$ suspension in the electrolyte (Fig. 4a) and promoted surface adsorption of $Li^+$ onto the $Li_2O$ surface (Fig. 3c). Also, the features of $Li_2O$-rich[30] SCE-SEI (Fig. 2f,h and Supplementary Fig. 1), inorganic-rich SCE-iSEI (Fig. 4d) and thin SCE-SEI (Fig. 2d) further support the decrease of the interfacial impedance of $Li^0$ with SCE. More importantly, the magnitude of the interfacial impedance decrease per $Li_2O$ suspension content in SCE was different, exhibiting a minor decrease in the interfacial impedance of $Li^0$ above 7 wt% $Li_2O$ SCE (Fig. 4e). As the $Li^+$

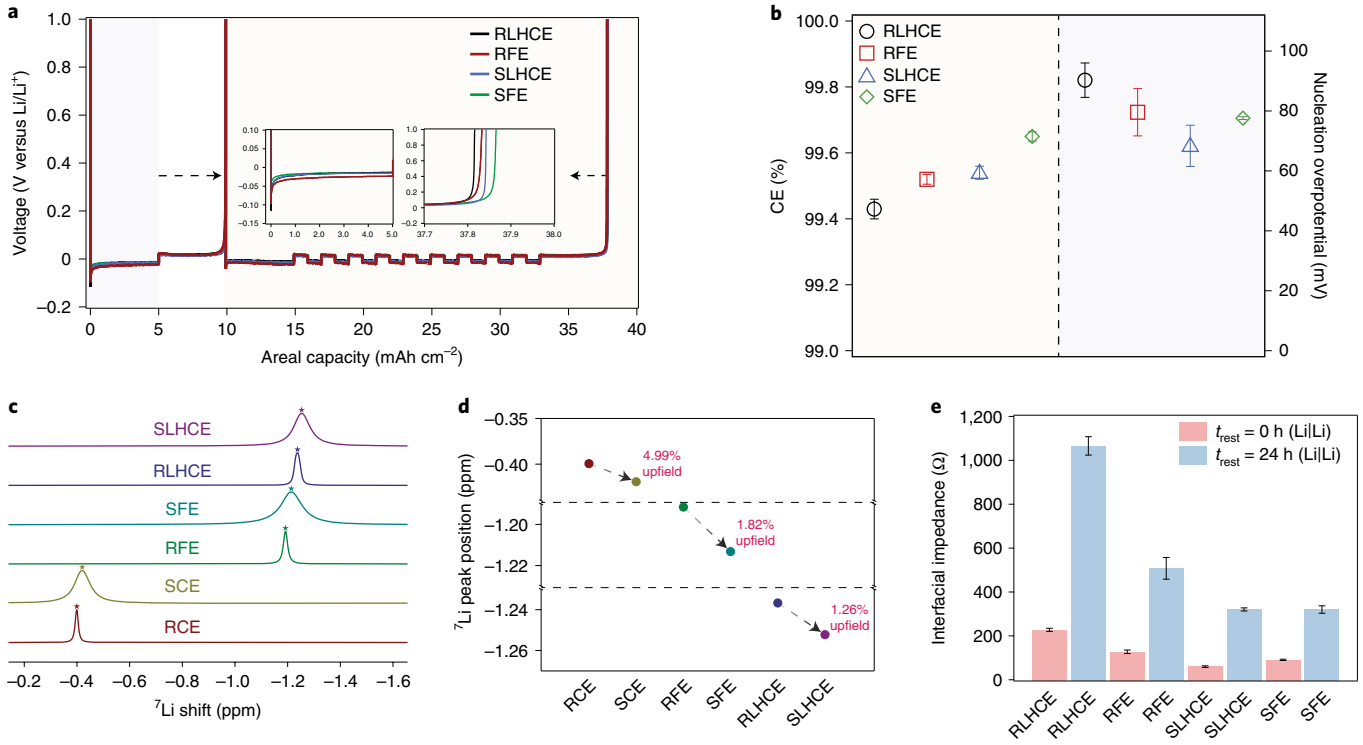


**Fig. 5 | High-performance electrolytes with the suspension electrolyte design. a**, Representative voltage profiles from Li|Cu cells with RLHCE, RFE, SLHCE and SFE for measuring CE and nucleation overpotential at 0.5 mA cm$^{-2}$. The insets show magnified initial and final voltage profiles to express clearer comparisons among the tested electrolytes. **b**, Averaged CE and nucleation overpotential values from four identical Li|Cu cells with RLHCE, RFE, SLHCE and SFE. The background colours represent the regions where CE and nucleation overpotential were calculated from **a**. The averaged CE and nucleation overpotential values of the electrolytes with standard errors are RLHCE (99.43 ± 0.03% and 90.27 ± 5.75 mV), RFE (99.52 ± 0.015% and 79.57 ± 7.87 mV), SLHCE (99.54 ± 0.02% and 68.37 ± 6.88 mV) and SFE (99.65 ± 0.014% and 77.63 ± 0.47 mV). **c**, The $^{7}$Li NMR spectra of RCE, SCE, RFE, SFE, RLHCE and SLHCE. **d**, The $^{7}$Li NMR peak positions retrieved from **c** for RCE, SCE, RFE, SFE, RLHCE and SLHCE. The relative peak shifts are indicated with the arrows between the points. **e**, The interfacial impedance of Li|Li cells with RLHCE, RFE, SLHCE and SFE measured at $t_{rest}$ = 0 h and $t_{rest}$ = 24 h. The $t_{rest}$ value represents the cell resting time after cell assembly. Three identical samples were measured to obtain averaged interfacial impedance values with standard errors.

solvation environment was affected by the $Li_2O$ suspension content (Fig. 4a–c and Supplementary Figs. 9 and 10), the interfacial impedance decrease (Fig. 4e) based on the $Li_2O$ suspension content was in line with the $Li^+$ solvation environment changes observed in $^{7}$Li NMR (Fig. 4b,c).

Moreover, monitoring temporal characteristics of interphases formed with a particular electrolyte on $Li^0$ became crucial due to the ageing of $Li^0$, which results in increased interfacial impedances of the $Li^0$ anode over time[10]. Thus, the interfacial impedances of $Li^0$ were measured with RCE and ~1–20 wt% $Li_2O$ SCE after 24 hours of cell assembly with respect to the suspension contents (Fig. 4f, Supplementary Fig. 17 and Supplementary Table 2). The change of the interfacial impedance in the suspension electrolytes became a weak function of time, indicating stable temporal characteristics of the interphases of $Li^0$ formed with SCE. Furthermore, the magnitude of the change in the interfacial impedance became smaller above 7 wt% $Li_2O$, which supports the optimal suspension content and thereby the optimal $Li^+$ solvation change effect, observed in Fig. 4b,e. Nyquist plots (Supplementary Fig. 17) for the impedance measurements in Fig. 4f demonstrate that electrolyte conductivity does not change with time, further supporting the stability of SCE and the interphases of $Li^0$ formed with SCE.

For the electrodes involving reactive materials such as $Li^0$, the large variation in the interfacial impedance after the electrochemical processes suggests that the system undergoes a more dynamic evolution and potentially unstable electrochemical processes. To illustrate this point, the interfacial impedances were measured from Li|Cu cells before and after $Li^0$ electrodeposition with RCE and SCE (Fig. 4g, Supplementary Fig. 18 and Supplementary Table 3). The change of the interfacial impedance after $Li^0$ electrodeposition was smaller for SCE than for RCE (Fig. 4g). To corroborate the electrochemical stability during the $Li^+$ migration, the voltage responses deduced from the repeated galvanostatic $Li^0$ plating/stripping with RCE and SCE certify that SCE allowed more stabilized $Li^+$ migration as less voltage hysteresis was achieved with SCE than with RCE (Supplementary Fig. 19).

## Suspensions in high-performance electrolytes

We further extended the suspension electrolyte design to validate its effect on the high-performance electrolytes (RFE and RLHCE). The CE measurements were performed with RLHCE, RFE, SLHCE and SFE to observe the CE and nucleation overpotential (Fig. 5a). The averaged values of CE and nucleation overpotential for the electrolytes are summarized in Supplementary Table 4. Both SFE and SLHCE exhibited improved CEs and reduced nucleation overpotentials (Fig. 5b), for which the suspension electrolyte design enabled further improvements for the high-performance electrolytes. To vividly portray the CE improvements of the carbonate (RCE) and high-performance electrolytes (RFE and RLHCE) with the suspension electrolyte design, the percent decrease in averaged Coulombic inefficiencies ($CI_{avg}$ decrease) were calculated (Supplementary Note 16 with Supplementary Fig. 20). The $Li^0$ electrodeposits with SFE (Supplementary Fig. 21) and SLHCE (Supplementary Fig. 22) were examined to understand the improved CE and reduced nucleation

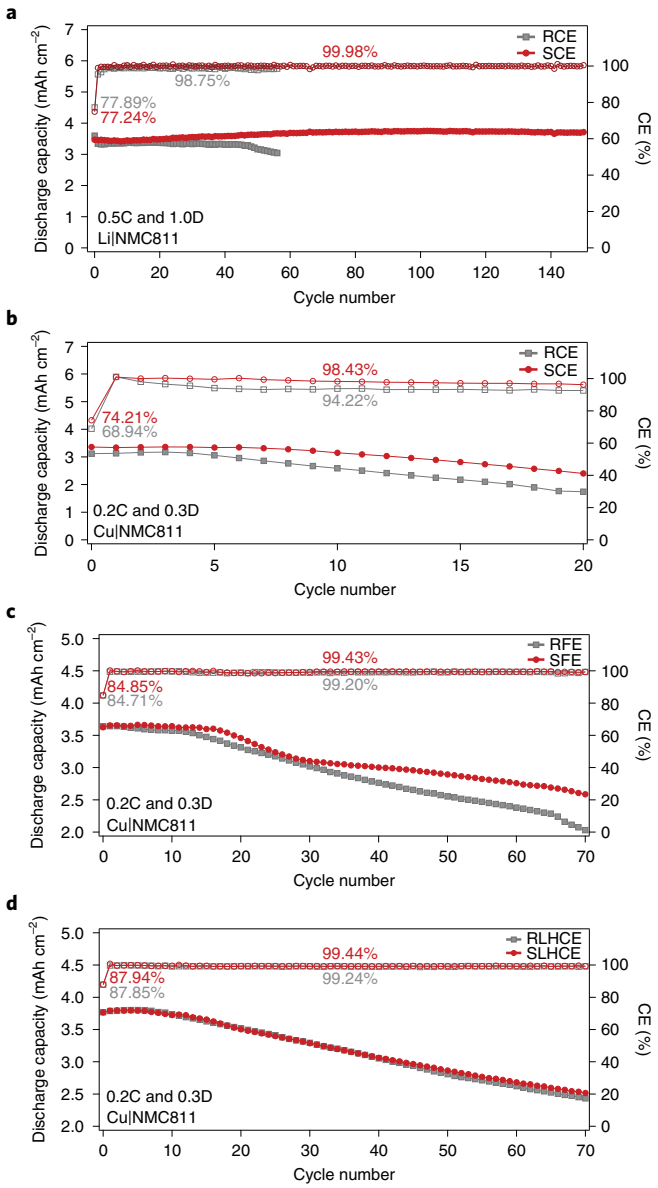


**Fig. 6 | Full cell electrochemical performances of the suspension electrolytes. a**, Representative Li|NMC811 full cell cycling profiles of the discharge capacity (filled symbols) and CE (open symbols) with RCE and SCE. The cycling was performed at 0.5C and 1.0D, where the C and D represent charging and discharging C rates, with the voltage window of 3.0–4.3 V versus $Li/Li^+$. The first cycle CE and the CE averaged over the rest of the cycle are displayed for RCE and SCE. **b**, Representative anode-free Cu|NMC811 cell cycling profiles of the discharge capacity (filled symbols) and CE (open symbols) with RCE and SCE. The cycling was performed at 0.2C and 0.3D with the voltage window of 3.0–4.3 V versus $Li/Li^+$. The first cycle CE and CE averaged over the rest of the cycle are displayed for RCE and SCE. **c**, Representative anode-free Cu|NMC811 cell cycling profiles of the discharge capacity (filled symbols) and CE (open symbols) with RFE and SFE. The cycling was performed at 0.2C and 0.3D with the voltage window of 3.0–4.3 V versus $Li/Li^+$. The first cycle CE and CE averaged over the rest of the cycle are displayed for RFE and SFE. **d**, Representative anode-free Cu|NMC811 cell cycling profiles of the discharge capacity (filled symbols) and CE (open symbols) with RLHCE and SLHCE. The cycling was performed at 0.2C and 0.3D with the voltage window of 3.0–4.3 V versus $Li/Li^+$. The first cycle CE and CE averaged over the rest of the cycle are displayed for RLHCE and SLHCE.

overpotential. As evidenced in Supplementary Fig. 21, denser and bulkier $Li^0$ electrodeposits were shown for SFE than for RFE. Equivalently, the $Li^0$ electrodeposits with SLHCE were also bulkier and more compact than with RLHCE (Supplementary Fig. 22).

The $^7Li$ NMR spectra were examined to observe the $Li^+$ solvation environment of SLHCE, RLHCE, SFE, RFE, SCE and RCE (Fig. 5c). The peak positions for the high-performance electrolytes (SLHCE, RLHCE, SFE and RFE) were in the upfield region, meaning the solvated $Li^+$ in the high-performance electrolytes has a higher electron density than in SCE and RCE. It has been reported that the $Li^+$ solvation shells of the high-performance electrolytes contain a relatively large amount of contact ion pairs and ionic aggregates[5,15,21]. Therefore, the peaks for the high-performance electrolytes were expected to be in the upfield region relative to RCE and SCE. The relative peak shifts based on SCE (4.99%), SFE (1.82%) and SLHCE (1.26%) are summarized in Fig. 5d. It was observed that the relative peak shift was the greatest for SCE and the least for SLHCE; the trends observed in $CI_{avg}$ decrease percentages (Supplementary Fig. 20) agree with the $^7Li$ NMR analyses (Fig. 5d). This implies that the effect of the suspension may vary with the choice of electrolyte. Another apparent effect of the suspension is that all the suspension electrolytes exhibited the peak shifts in the upfield direction, suggesting that the suspension in the high-performance electrolytes has similar effects to those observed in SCE. To further clarify this point, XPS analyses were performed with high-performance electrolytes, which showed higher inorganic surface features of SLHCE-iSEI and SFE-iSEI than with RLHCE-iSEI and RFE-iSEI (Supplementary Note 17 with Supplementary Figs. 23–26).

The interfacial impedances of $Li^0$ with the high-performance electrolytes were measured to analyse the electrochemical effect of the $Li_2O$ suspension in the high-performance electrolytes (Fig. 5e, Supplementary Fig. 27 and Supplementary Table 5). Lower interfacial impedances of $Li^0$ were achieved with SLHCE and SFE relative to those with RLHCE and RFE (Fig. 5e). Also, the interfacial impedance changes before and after $Li^0$ electrodeposition (Supplementary Figs. 28 and 29) with SLHCE and SFE were smaller than with RLHCE and RFE. Therefore, the interphases that $Li^0$ forms with the suspension electrolytes (SCE, SFE and SLHCE) were favourable and electrochemically stable.

## Full cell performances with the suspension electrolytes

The suspension electrolytes were paired with a $LiNi_{0.8}Mn_{0.1}Co_{0.1}$ (NMC811) cathode to construct Li|NMC811 and Cu|NMC811 full cells (Fig. 6). Li|NMC811 cells with a large excess of $Li^0$ anode and an electrolyte loading of 5 µl $mAh_{NMC811}^{-1}$ were cycled between 3.0 V and 4.3 V versus $Li/Li^+$ with RCE and SCE (Fig. 6a). These parameters were chosen to observe the cell failure restricted by the electrolyte depletion or impedance build-up in the electrode of the cells, which largely depend on the electrolyte performance. Li|NMC811 full cells (Fig. 6a) with SCE cycled at 0.5 C charging (0.5C) and 1.0 C discharging (1.0D) rates exhibited prolonged cycle life compared to that of RCE. This improvement signifies that the electrolyte consumption and/or the rate of undesired interfacial impedance build-up during the cycling were relatively reduced with SCE. Although the theoretical oxidation potential of $Li_2O$ (3.1 V versus $Li/Li^+$)[42] is lower than the operating potential of NMC811 (3.0–4.3 V versus $Li/Li^+$), the suspension electrolyte design enabled the stable cycling of the $Li_2O$ suspension in the full cell up to 4.5 V versus $Li/Li^+$ (Supplementary Note 18 with Supplementary Figs. 30 and 31). Also, the cycling characteristics of the suspension electrolyte in the full cell exhibited a weak dependency on gravity, cell orientations and suspension blocking the pores of the separator (Supplementary Note 19 with Supplementary Figs. 31 and 32).

With the specific aim of verifying our suspension electrolyte design under more realistic conditions for practical LMBs, we explored the cycling performance of the suspension electrolytes in

the anode-free (Cu|NMC811) cell configuration with a lean electrolyte loading of 2.5 µl $mAh_{NMC811}^{-1}$. The cycling performance of Cu|NMC811 with SCE at 0.2C and 0.3D exhibited a 5.27% higher first cycle CE and 4.21% higher cycling CE from the second to the 20th cycle with improved capacity retentions, compared with that of RCE (Fig. 6b). The cycling voltage profiles of RCE and SCE (Supplementary Fig. 33) indicate that active $Li^0$ was stably utilized over the cycles, as cycling voltage profiles of the cell with SCE showed a constant slope of charging voltage curves and constant-voltage charging profile length[43,44], whereas increased voltage-curve slopes and lengthened constant-voltage profiles were shown with RCE. The cycling profiles of the anode-free cells with RFE and SFE at 0.2C and 0.3D are shown in Fig. 6c, where improved CE and capacity retentions were obtained with SFE. In a similar manner, stabilized charge/discharge voltage profiles were also achieved with SFE (Supplementary Fig. 34). Interestingly, although improved overall CEs of SLHCE were observed (Fig. 6d and Supplementary Fig. 35), the degree of the performance improvement was not as much as in SCE and SFE. This could be realized from the least peak shift observed in $^7Li$ NMR (Fig. 5d) and $CI_{avg}$ decrease (Supplementary Fig. 20), in which the impact of the suspension in the $Li^+$ solvation change and CE improvement was least for SLHCE. The full cell cycling profiles with multiple cells are shown in Supplementary Fig. 36. Moreover, detailed explanations are provided in Supplementary Note 20 to correlate the mechanism of the suspension electrolyte to the electrochemical performance improvement of the $Li^0$ anode. The possible factors that may affect the suspension electrolytes and future insights are discussed in Supplementary Note 21 with Supplementary Fig. 37.

## Conclusions

In this work, we present a suspension electrolyte design to derive favourable SEIs on $Li^0$ for LMBs. $Li_2O$-based suspension electrolytes were investigated in detail as proof of concept. We found that the addition of $Li_2O$ into the liquid electrolytes resulted in improved CE, reduced nucleation overpotential, stabilized $Li^0$ interphase and improved electrochemical performances in full cells. Moreover, the suspension electrolyte design has been extended to state-of-the-art high-performance electrolytes to confirm that the suspension electrolytes are not limited to a particular electrolyte system. Most importantly, we were able to determine essential roles played by $Li_2O$ in the liquid electrolyte employing the suspension electrolyte design. Hence, the suspension electrolyte design potentially serves as a useful study platform to closely observe explicit features of the inorganics that are essential to the SEIs for LMBs. We expect the suspension electrolyte design to evolve into a better understanding of (1) inorganics in SEIs for the $Li^0$ anode, (2) a facile and universal strategy for designing electrolytes and (3) modifying the $Li^+$ solvation environment to derive favourable SEIs on the $Li^0$ anode to develop reliable LMBs.

## Online content

Any methods, additional references, Nature Research reporting summaries, source data, extended data, supplementary information, acknowledgements, peer review information; details of author contributions and competing interests; and statements of data and code availability are available at https://doi.org/10.1038/s41563-021-01172-3.

Received: 11 August 2021; Accepted: 18 November 2021;
Published online: 17 January 2022

## References

1. Xiao, J. et al. Understanding and applying Coulombic efficiency in lithium metal batteries. *Nat. Energy* **5**, 561–568 (2020).
2. Zheng, J. et al. Regulating electrodeposition morphology of lithium: towards commercially relevant secondary Li metal batteries. *Chem. Soc. Rev.* **49**, 2701–2750 (2020).
3. Liu, J. et al. Pathways for practical high-energy long-cycling lithium metal batteries. *Nat. Energy* **4**, 180–186 (2019).
4. Lin, D., Liu, Y. & Cui, Y. Reviving the lithium metal anode for high-energy batteries. *Nat. Nanotechnol.* **12**, 194–206 (2017).
5. Wu, H., Jia, H., Wang, C., Zhang, J. G. & Xu, W. Recent progress in understanding solid electrolyte interphase on lithium metal anodes. *Advanced Energy Materials* **11**, 2003092 (2021).
6. Zachman, M. J., Tu, Z., Choudhury, S., Archer, L. A. & Kourkoutis, L. F. Cryo-STEM mapping of solid–liquid interfaces and dendrites in lithium-metal batteries. *Nature* **560**, 345–349 (2018).
7. Li, Y. et al. Correlating structure and function of battery interphases at atomic resolution using cryoelectron microscopy. *Joule* **2**, 2167–2177 (2018).
8. Li, Y. et al. Atomic structure of sensitive battery materials and interfaces revealed by cryo–electron microscopy. *Science* **358**, 506–510 (2017).
9. Shadike, Z. et al. Identification of LiH and nanocrystalline LiF in the solid–electrolyte interphase of lithium metal anodes. *Nat. Nanotechnol.* https://doi.org/10.1038/s41565-020-00845-5 (2021).
10. Boyle, D. T. et al. Corrosion of lithium metal anodes during calendar ageing and its microscopic origins. *Nat. Energy* https://doi.org/10.1038/s41560-021-00787-9 (2021).
11. Xu, K. Electrolytes and interphases in Li-ion batteries and beyond. *Chem. Rev.* **114**, 11503–11618 (2014).
12. Cao, X. et al. Monolithic solid–electrolyte interphases formed in fluorinated orthoformate-based electrolytes minimize Li depletion and pulverization. *Nat. Energy* **4**, 796–805 (2019).
13. Fan, X. et al. Non-flammable electrolyte enables Li-metal batteries with aggressive cathode chemistries. *Nat. Nanotechnol.* **13**, 715–722 (2018).
14. Zhang, X. Q. et al. Regulating anions in the solvation sheath of lithium ions for stable lithium metal batteries. *ACS Energy Lett.* **4**, 411–416 (2019).
15. Yu, Z. et al. Molecular design for electrolyte solvents enabling energy-dense and long-cycling lithium metal batteries. *Nat. Energy* **5**, 526–533 (2020).
16. Yuan, S. et al. Salt-rich solid electrolyte interphase for safer high-energy-density Li metal batteries with limited Li excess. *Chem. Commun.* **56**, 8257–8260 (2020).
17. Yamada, Y., Wang, J., Ko, S., Watanabe, E. & Yamada, A. Advances and issues in developing salt-concentrated battery electrolytes. *Nat. Energy* **4**, 269–280 (2019).
18. Fan, X. et al. Highly fluorinated interphases enable high-voltage Li-metal batteries. *Chem* **4**, 174–185 (2018).
19. Qian, J. et al. High rate and stable cycling of lithium metal anode. *Nat. Commun.* **6**, 6362 (2015).
20. Suo, L. et al. "Water-in-salt" electrolyte enables high-voltage aqueous lithium-ion chemistries. *Science* **350**, 938–943 (2015).
21. Ren, X. et al. Enabling high-voltage lithium-metal batteries under practical conditions. *Joule* **3**, 1662–1676 (2019).
22. Chen, S. et al. High-voltage lithium-metal batteries enabled by localized high-concentration electrolytes. *Adv. Mater.* **30**, 1706102 (2018).
23. Chen, S. et al. High-efficiency lithium metal batteries with fire-retardant electrolytes. *Joule* **2**, 1548–1558 (2018).
24. Amanchukwu, C. V., Kong, X., Qin, J., Cui, Y. & Bao, Z. Nonpolar alkanes modify lithium-ion solvation for improved lithium deposition and stripping. *Advanced Energy Materials* **9**, 1902116 (2019).
25. Tasaki, K. et al. Solubility of lithium salts formed on the lithium-ion battery negative electrode surface in organic solvents. *J. Electrochem. Soc.* **156**, A1019 (2009).
26. Huang, W., Wang, H., Boyle, D. T., Li, Y. & Cui, Y. Resolving nanoscopic and mesoscopic heterogeneity of fluorinated species in battery solid-electrolyte interphases by cryogenic electron microscopy. *ACS Energy Lett.* **5**, 1128–1135 (2020).
27. Liu, Y. et al. Solubility-mediated sustained release enabling nitrate additive in carbonate electrolytes for stable lithium metal anode. *Nat. Commun.* **9**, 3656 (2018).
28. Wang, J. et al. Improving cyclability of Li metal batteries at elevated temperatures and its origin revealed by cryo-electron microscopy. *Nat. Energy* **4**, 664–670 (2019).
29. Lowe, J. S. & Siegel, D. J. Modeling the interface between lithium metal and its native oxide. *ACS Appl. Mater. Interfaces* **12**, 46015–46026 (2020).
30. Guo, R. & Gallant, B. M. $Li_2O$ solid electrolyte interphase: probing transport properties at the chemical potential of lithium. *Chem. Mater.* https://doi.org/10.1021/acs.chemmater.0c00333 (2020).
31. Tan, L. et al. In-situ tailored 3D $Li_2O$@Cu nanowires array enabling stable lithium metal anode with ultra-high coulombic efficiency. *J. Power Sources* **463**, 228178 (2020).
32. Shen, C. et al. Li2O-reinforced solid electrolyte interphase on three-dimensional sponges for dendrite-free lithium deposition. *Front. Chem.* **6**, 517 (2018).

33. Adams, B. D., Zheng, J., Ren, X., Xu, W. & Zhang, J. G. Accurate determination of Coulombic efficiency for lithium metal anodes and lithium metal batteries. *Adv. Energy Mater.* **8**, 1702097 (2017).
34. Kim, M. S. et al. Langmuir–Blodgett artificial solid-electrolyte interphases for practical lithium metal batteries. *Nat. Energy* **3**, 889–898 (2018).
35. Pei, A., Zheng, G., Shi, F., Li, Y. & Cui, Y. Nanoscale nucleation and growth of electrodeposited lithium metal. *Nano Lett.* **17**, 1132–1139 (2017).
36. Fister, T. T. et al. Electronic structure of lithium battery interphase compounds: comparison between inelastic X-ray scattering measurements and theory. *J. Chem. Phys.* **135**, 224513 (2011).
37. Ozhabes, Y., Gunceler, D. & Arias, T. A. Stability and surface diffusion at lithium-electrolyte interphases with connections to dendrite suppression. Preprint at *arXiv* https://arxiv.org/abs/1504.05799 (2015).
38. Lu, Y., Tu, Z. & Archer, L. A. Stable lithium electrodeposition in liquid and nanoporous solid electrolytes. *Nat. Mater.* **13**, 961–969 (2014).
39. Kim, S. C. et al. Potentiometric measurement to probe solvation energy and its correlation to lithium battery cyclability. *J. Am. Chem. Soc.* **143**, 10301–10308 (2021).
40. Amanchukwu, C. V. et al. A new class of ionically conducting fluorinated ether electrolytes with high electrochemical stability. *J. Am. Chem. Soc.* **142**, 7393–7403 (2020).
41. Kamphaus, E. P. et al. Role of inorganic surface layer on solid electrolyte interphase evolution at Li-metal anodes. *ACS Appl. Mater. Interfaces* **11**, 31467–31476 (2019).
42. Xie, J. et al. Atomic layer deposition of stable $LiAlF_4$ lithium ion conductive interfacial layer for stable cathode cycling. *ACS Nano* **11**, 7019–7027 (2017).
43. Kim, M. S. et al. Enabling reversible redox reactions in electrochemical cells using protected LiAl intermetallics as lithium metal anodes. *Sci. Adv.* https://doi.org/10.1126/sciadv.aax5587 (2019).
44. Kim, M. S. et al. Langmuir–Blodgett artificial solid-electrolyte interphases for practical lithium metal batteries. *Nat. Energy* https://doi.org/10.1038/s41560-018-0237-6 (2018).

## Methods

**Materials.** All the electrolytes were prepared and made in an Ar-filled glove box with an $O_2$ concentration below 0.2 ppm and $H_2O$ concentration below 0.01 ppm. The RCE was prepared with 1 M $LiPF_6$ in EC/DEC (1:1 v/v; Gotion LP 40) with 10 vol% FEC (BASF). The RFE was prepared with 1 M LiFSI (Oakwood) in FDMB. The FDMB was synthesized by following a previous method[15]. The RLHCE was prepared with 1 M LiFSI (Oakwood) in TTE (Synquest Laboratories)/DME (Sigma-Aldrich; 0.78:0.22 v/v). $Li_2O$ nanoparticles (~80–100 nm in diameter) were used and purchased from Nanoshel. $Li_2O$ microparticles (100 mesh) were used and purchased from Alfa-Aeser. SCE, SFE and SLHCE were prepared by dispersing 7 wt% $Li_2O$ and about 5.9% volume ratio of $Li_2O$ versus electrolyte (otherwise indicated) into RCE, RFE and RLHCE. All the suspension electrolytes were freshly made by mixing dried $Li_2O$ nanoparticles or microparticles (stored inside of the glove box) with fresh liquid electrolyte right before the measurements. DME, dioxolane (DOL) and DEC were purchased from Sigma-Aldrich to perform the solvation energy measurements. High-purity Li foil (500 µm, 99.9%; Alfa Aesar), Cu foil (Pred Materials), 11 µm polyethylene separator (W-Scope) and NMC811 (Targray) were used to make 2032-type coin cells.

**MD simulations.** MD simulations were carried out using Gromacs 2018 (ref. [45]), with electrolyte molar ratios taken from those used in the experimental work. Molecular forces were calculated using the Optimized Potentials for Liquid Simulations all atom (OPLS-AA) force field[46]. Topology files and bonded and Lennard-Jones parameters for carbonates were generated using the LigParGen server[47], while parameters for $PF_6^-$ and $Li_2O$ were taken from the literature[48,49]. Atomic partial charges for carbonates and $PF_6^-$ were calculated by fitting the molecular electrostatic potential at atomic centres in Gaussian16 using the Møller–Plesset second-order perturbation method with a cc-pVTZ basis set. The simulation procedure for the bulk electrolyte (analogous to the RCE) consists of an energy minimization using the steepest descent method followed by a 4 ns equilibration step using a Berendsen barostat and a 20 ns production run using a Parrinello–Rahman barostat, both at a reference pressure of 1 bar. A Nosé–Hoover thermostat was used throughout with a reference temperature of 300 K. The particle mesh Ewald method was used to calculate electrostatic interactions, with a real-space cut-off of 0.12 nm and a Fourier spacing of 0.12 nm. The Verlet cut-off scheme was used to generate pair lists. A cut-off of 0.12 nm was used for non-bonded Lennard-Jones interactions. Periodic boundary conditions were applied in all directions. Bonds with hydrogen atoms were constrained. Convergence of the system energy, temperature and box size were checked to verify equilibration. The final 10 ns of the production run were used to generate results.

Simulations were also carried out with a lithium oxide slab to understand the effect of the oxide suspension. The (111) surface was modelled, as it is reported to be the most stable surface[50]. The slab was approximately 1.2 nm thick to ensure screening of any unphysical interactions between liquid electrolytes on either side of the slab. The slabs were observed to be structurally stable over the course of the simulation; however, to ensure accurate simulation of the ordered crystalline structure, positional restraints were also implemented for atoms in the slab with a force constant of 1,000 kJ $mol^{-1}$ $nm^{-2}$. For simulations with the slab, the system was made incompressible in the $x$ and $y$ directions but allowed to compress in the $z$ direction (perpendicular to the slab). A relatively long simulation box was used (approximately 17 nm in the $z$ direction after equilibration relative to approximately 5 nm in the $x$ and $y$ dimensions) to ensure that conditions far from the slab matched those in the RCE simulation. Other details of the simulations with lithium oxide matched those of the RCE simulations except that the equilibration step was lengthened to 10 ns. Simulations conducted without the use of positional restraints yielded similar results.

Density profiles and RDFs were generated using Gromacs, while visualizations were generated with VMD[51]. Solvation shell statistics were calculated using the MDAnalysis Python package[52] by histogramming the observed first solvation shells for lithium ions during the production simulation, using a method similar to previous work[15]. A cut-off distance of 0.5 nm from the surface for lithium ions was chosen to evaluate the solvation shells near the surface in order to capture the observed lithium adsorption peak in the density profile near the surface. The solvent shell calculations for 'near' the surface were defined as the shell of any lithium ion within 0.5 nm of the surface. Therefore, some solvent or counterions farther from the surface would have been counted, but the lithium ions were within 0.5 nm. The cut-off for each species in the first Li solvation shell was calculated from the first minimum occurring in the RDF (referenced to lithium ions) after the initial peak.

**DFT simulations.** The calculations were performed with the DFT code GPAW[53–55]. The Perdew–Burke–Ernzerhof[56] functional within the generalized gradient approximation was used to describe the electron exchange–correlation effect. Plane-wave basis sets and the projector augmented-wave method were used for electronic wavefunctions. The energy cut-off of 450 eV was applied to all the calculations. The $k$-point grid of $2\times2\times1$ was used for $Li_2O$ slab calculations. The energy and forces per atom were converged to within $10^{-4}$ eV and $10^{-3}$ eV $Å^{-1}$, respectively. For the slab calculations, the vacuum thickness was chosen to be 15 Å to reduce artificial interactions due to periodic boundary conditions. The $Li_2O$ slab consisted of six layers of unit cells (spanning approximately 15 Å) in the $z$ direction. For Li adsorption calculations, atoms below the top four atomic layers were constrained during geometry optimization.

**Characterizations.** *Cryo-STEM and SEM.* For TEM sample preparation, Cu TEM grids were used as the working electrode for Li metal plating. A total capacity of 0.1 mAh $cm^{-2}$ was deposited under a constant current of 1 mA $cm^{-2}$. The Li/Cu TEM grid coin cells were disassembled in an argon-filled glove box. TEM grids were rinsed with 60 µl of pure DEC to remove residual salts and dried before freezing. Then, the TEM grid was sealed in an airtight container, which was immediately submerged and crushed in liquid nitrogen to rapidly expose the sample to cryogen without air exposure.

For cryo-STEM characterization, while immersed in liquid nitrogen, the sample was loaded into the Gatan side-entry cryo-transfer holder (Gatan model 626) and inserted into the TEM column. The cryo-STEM/TEM holder uses a specialized cryo-shutter to prevent air exposure and ice condensation onto the sample. Once inside the TEM column, the temperature was maintained at approximately −178 °C.

Cryo-STEM experiments were performed on a Thermofisher Titan 80–300 environmental (scanning) transmission electron microscope operated at an accelerating voltage of 300 kV. The instrument is equipped with an aberration corrector in the image-forming lens, which was tuned before each sample analysis. Cryo-TEM images were acquired by a Gatan K3 IS direct-detection camera in electron-counting mode. Cryo-STEM/TEM images were taken with an electron dose rate of around 100 $e^-$ $Å^{-2}$ $s^{-1}$, and a total of five frames were taken with 0.1 s per frame for each image.

Cryo-STEM EELS characterization was performed with a C2 aperture of 50 mm, a probe current of 75 pA, a camera length of 38 mm and a pixel dwell time of 100 ms. EELS spectra were acquired on a high-resolution Gatan imaging filter (GIF Quantum 966) with a dispersion of 0.25 eV per channel in dual EELS mode. Maps were computed through a two-window method, with a pre-edge window fitted to a power-law background and a post-edge window of 20–40 eV on the core-loss signal.

*Solvation energy measurements.* Please refer to the literature[39] for the detailed apparatus set-up. In brief, 1 M LiFSI in DEC and 3 M LiFSI in DME/DOL were used for $EL_{ref}$ and the salt bridge, respectively. RCE, 20 wt% $Li_2O$ nanoparticles in SCE, and 20 wt% $Li_2O$ microparticles in RCE were used for $EL_{test}$. The cell potentials were measured by Biologic VMP3 using the H-cell ($EL_{ref}$|salt-bridge|$EL_{test}$) with Li electrodes in contact with $EL_{ref}$ and $EL_{test}$. The cell potentials were measured for each of the $EL_{test}$; the cell potentials and solvation energies were recorded for 3 seconds; and averaged values were reported.

*The $^7$Li NMR spectroscopy.* A capillary tube insert sealed with a polytetrafluoroethylene cap was used for NMR experiments. The outer tube contained freshly prepared suspension electrolyte and the inner tube contained 1 M LiCl in $D_2O$ as an external reference. The $^7$Li NMR was performed on a Varian Inova 500 MHz NMR instrument. The external reference was used for locking and shimming. The chemical shifts were referenced to 1 M LiCl in $D_2O$ at 0 ppm.

*XPS.* The characterization was performed on a PHI Versaprobe I with a monochromatized Al Kα X-ray source. The chamber was kept at a pressure of about $10^{-7}$ Pa during characterization. High-purity Li foil (750 µm, 99.9%; Alfa Aesar) was used. Prior to characterization, the Li surface was rinsed with 60 µl of pure solvent (DEC for carbonate-based electrolytes and DME for ether-based electrolytes) in an Ar-filled glove box to remove residual salt. A vacuum transfer vessel was used to transfer the samples directly from the Ar glove box to the vacuum transfer chamber of the instrument to prevent air exposure. High-resolution spectra were calibrated using the C 1*s* peak at 284.6 eV.

*Electrochemical measurements.* Three reference (RCE, RFE and RLHCE) and three suspension (SCE, SFE and SLHCE) electrolytes were used in this study. For Li|Cu, Li|Li and Li|NMC811 cells, 20 µl of the specified electrolytes were used. For Cu|NMC811 cells, 10 µl of the specified electrolytes were used. Electrochemical impedance spectroscopy was measured by Biologics VMP3 with the frequency ranging from 7 MHz to 100 mHz. Cyclic voltammetry was measured by Biologics VMP3 with a scan rate of 0.1 mV $s^{-1}$ and voltage window of 3–4.5 V versus Li/$Li^+$ using RCE and SCE in Li|NMC811 cells. Linear sweep voltammetry was measured by Biologics VMP3 with a scan rate of 1 mV $s^{-1}$ and voltage window of 3–5 V versus Li/$Li^+$ using RCE and SCE in Li|Al cells. For Li|Cu, Li|Li and Li|NMC811 cells, the measurements were done by Arbin and Land instruments. For CE and nucleation overpotential measurements from Li|Cu cells, a current density of 0.05 mA $cm^{-2}$ was used with a cut-off voltage of 1 V versus Li/$Li^+$ to cycle. For Li|NMC811 and Cu|NMC811 cells, specified charging and discharging C rates were used with the voltage window of 3.0–4.3 V versus Li/$Li^+$, where the constant current goes up to 4.2 V versus Li/$Li^+$ and the constant voltage was held at 4.3 V versus Li/$Li^+$, with the cut-off current value of 0.05 C. Galvanostatic charging up to 4.2 V versus Li/$Li^+$ was considered to closely observe the performance impact of the $Li^0$ anode in the full cells over the cycles as the NMC811 cathode runs relatively stably between 3 V

and 4.2 V versus Li/Li$^+$. In this way, it becomes easier to decouple the impact of the electrochemical performance between the Li$^0$ anode and NMC811 cathode. The constant-voltage charging at 4.3 V versus Li/Li$^+$ was considered to extract more capacity from the cathode as the NMC811 cathode exhibits a higher capacity by charging up to 4.3 V than up to 4.2 V versus Li/Li$^+$.

*Elemental analysis.* The electrochemical framework of the Li|NMC811 cell was established based on the theory developed by Newman et al. The ion (including cations and anions) flux in the electrolyte constitutes the electric field between two electrodes, which alters the movement of suspension particles by the dielectrophoretic force

$$\mathbf{F}_{\mathrm{E}} = \frac{\pi}{4}\left(\frac{\varepsilon_{\mathrm{P}} - 1}{\varepsilon_{\mathrm{P}} + 2}\right)\varepsilon_{\mathrm{P}} d_{\mathrm{P}}^3 \mathrm{grad}\,\mathbf{E}^2$$

where $\mathbf{F}_{\mathrm{E}}$ is the dielectrophoretic force acting on the particles, $\varepsilon_{\mathrm{P}}$ is the dielectric constant of particles, $d_{\mathrm{P}}$ is the particle diameter and $\mathbf{E}$ is the electric field. Since the particle size is in the nanoscale, the Brownian force also affects to the particle movement:

$$\mathbf{F}_{\mathrm{B}} = \tilde{\mathbf{I}}\sqrt{\frac{6\pi k_{\mathrm{B}} \mu T d_{\mathrm{P}}}{\Delta t}}$$

where $\mathbf{F}_{\mathrm{B}}$ is the Brownian force acting on the particles, $\tilde{\mathbf{I}}$ is the random directional unit vector, $k_{\mathrm{B}}$ is the Boltzmann's constant, $T$ is the electrolyte temperature, $\mu$ is the electrolyte viscosity and $\Delta t$ is the size of the time step taken by the solver. All the numerical simulation was performed using commercial software COMSOL Multiphysics. The geometrical and electrochemical parameters in the numerical model are set to be consistent with the experimental set-up.

## Data availability

The authors declare that all the data and relevant information are available within the article and Supplementary Information. Additional data are available from the corresponding author upon reasonable request.

## Code availability

The MD and DFT simulation codes are available at https://github.com/prudnick94/LiSolvation_Li2OSuspension and https://github.com/exenGT/Li2O, respectively.

## References


45. Abraham, M. J. et al. Gromacs: high performance molecular simulations through multi-level parallelism from laptops to supercomputers. *SoftwareX* **1–2**, 19–25 (2015).
46. Jorgensen, W. L., Maxwell, D. S. & Tirado-Rives, J. Development and testing of the OPLS all-atom force field on conformational energetics and properties of organic liquids. *J. Am. Chem. Soc.* **118**, 11225–11236 (1996).
47. Dodda, L. S., De Vaca, I. C., Tirado-Rives, J. & Jorgensen, W. L. LigParGen web server: an automatic OPLS-AA parameter generator for organic ligands. *Nucleic Acids Res.* **45**, W331–W336 (2017).
48. Doherty, B., Zhong, X., Gathiaka, S., Li, B. & Acevedo, O. Revisiting OPLS force field parameters for ionic liquid simulations. *J. Chem. Theory Comput.* **13**, 6131–6135 (2017).
49. Benitez, L. & Seminario, J. M. Ion diffusivity through the solid electrolyte interphase in lithium-ion batteries. *J. Electrochem. Soc.* **164**, E3159–E3170 (2017).
50. Radin, M. D., Rodriguez, J. F., Tian, F. & Siegel, D. J. Lithium peroxide surfaces are metallic, while lithium oxide surfaces are not. *J. Am. Chem. Soc.* **134**, 1093–1103 (2012).
51. Humphrey, W., Dalke, A. & Schulten, K. VMD: Visual Molecular Dynamics. *J. Mol. Graph.* **14**, 33–38 (1996).
52. Allouche, A. Gabedit—a graphical user interface for computational chemistry softwares. *J. Comput. Chem.* **32**, 174–182 (2011).
53. Mortensen, J. J., Hansen, L. B. & Jacobsen, K. W. Real-space grid implementation of the projector augmented wave method. *Phys. Rev. B* **71**, 035109 (2005).
54. Enkovaara, J. et al. Electronic structure calculations with GPAW: a real-space implementation of the projector augmented-wave method. *J. Phys. Condens. Matter* **22**, 253202 (2010).
55. Hjorth Larsen, A. et al. The atomic simulation environment—a Python library for working with atoms. *J. Phys. Condens. Matter* **29**, 273002 (2017).
56. Perdew, J. P., Burke, K. & Ernzerhof, M. Generalized gradient approximation made simple. *Phys. Rev. Lett.* **77**, 3865–3868 (1996).


## Acknowledgements


We acknowledge support from the Assistant Secretary for Energy Efficiency and Renewable Energy, Office of Vehicle Technologies of the US Department of Energy under the Battery Materials Research Program and Battery 500 Consortium. Z.Z. acknowledges the support from the Stanford Interdisciplinary Graduate Fellowship. S.T.O. acknowledges support from the Knight Hennessy scholarship for graduate studies at Stanford University.


## Author contributions

M.S.K. and Y. Cui conceived the idea and conceptualized the work. M.S.K. performed the experiments and analysed the data with guidance from Y. Cui. M.S.K., Z.Z. and Y. Cui wrote the manuscript. Z.Z. performed cryo-STEM and SEM experiments and analyses. P.E.R. performed MD simulations and analysed the data. J.W. conducted DFT calculations. Z.Y. synthesized FDMB electrolyte and helped to take impedance measurements. S.T.O. performed XPS analysis. Y. Chen performed $^7$Li NMR analysis. S.C.K. measured the cell potential and relative Li$^+$ solvation energy of the electrolytes. W.Z. helped take SEM images. Z.Y., H.W., S.C.K., D.T.B., X.K., Z.H. and W.H. provided technical help and helpful discussions. S.F.B. and L.-W.W. reviewed the manuscript. Y. Cui, Z.B. and J.Q. supervised the overall study. All the authors discussed the manuscript and provided comments.

## Competing interests

The authors declare no competing interests.

## Additional information

**Supplementary information** The online version contains supplementary material available at https://doi.org/10.1038/s41563-021-01172-3.

**Correspondence and requests for materials** should be addressed to Yi Cui.